Geophysical Journal International

Geophys. J. Int. (2021) **226,** 1574–1583
Advance Access publication 2021 May 05
GJI General Geophysical Methods

doi: 10.1093/gji/ggab148

Induced polarization effects in airborne transient electromagnetic data collected in the McMurdo Dry Valleys, Antarctica

Denys Grombacher[1], Esben Auken,[1] Nikolaj Foged,[1] Thue Bording,[1] Neil Foley,[2] Peter T. Doran,[3] Jill Mikucki[4], Hilary A. Dugan[5], Ricardo Garza-Giron,[2] Krista Myers,[3] Ross A. Virginia[6] and Slawek Tulaczyk[2]

[1]*Department of Geoscience, Aarhus University,* 8000 *Aarhus, Denmark. E-mail: denys.grombacher@geo.au.dk*
[2]*Department of Earth and Planetary Sciences, University of California—Santa Cruz, Santa Cruz, CA* 95064*, USA*
[3]*Department of Geology and Geophysics, Louisiana State University, Baton Rouge, LA* 70802*, USA*
[4]*Department of Microbiology, University of Tennessee, Knoxville, TN* 37996*, USA*
[5]*Center for Limnology, University of Wisconsin—Madison, Madison, WI* 53706*, USA*
[6]*Environmental Studies Program, Dartmouth College, Hanover, NH* 03755-3541*, USA*

Accepted 2021 April 13. Received 2021 March 17; in original form 2020 July 27

SUMMARY

Airborne electromagnetics (EM) is a geophysical tool well suited to mapping glacial and hydrogeological structures in polar environments. This non-invasive method offers significant spatial coverage without requiring access to the ground surface, enabling the mapping of geological units to hundreds of metres depth over highly varied terrain. This method shows great potential for large-scale surveys in polar environments, as common targets such as permafrost, ice and brine-rich groundwater systems in these settings can be easily differentiated because of their significant contrasts in electrical properties. This potential was highlighted in a 2011 airborne EM survey in the McMurdo Dry Valleys that mapped the existence of a large-scale regional groundwater system in Taylor Valley. A more comprehensive airborne EM survey was flown in November 2018 to broadly map potential groundwater systems throughout the region. Data collected in this survey displayed significant perturbations from a process called induced polarization (IP), an effect that can greatly limit or prevent traditional EM workflows from producing reliable geological interpretations. Here, we present several examples of observed IP signatures over a range of conditions and detail how workflows explicitly designed to handle IP effects can produce reliable geological interpretations and data fits in these situations. Future polar EM surveys can be expected to encounter strong IP effects given the likely presence of geological materials (e.g. ice and permafrost) that can accentuate the influence of IP.

Key words: Hydrogeophysics; Antarctica; Electromagnetic theory.

INTRODUCTION

The McMurdo Dry Valleys in Antarctica are hyper-arid polar deserts (Marchant & Head 2007) and represent a significant portion of the snow- and ice-free regions on the continent (Gooseff *et al.* 2013). Despite the region's low mean annual temperatures and low precipitation (Doran *et al.* 2002), a 2011 airborne electromagnetic (AEM) survey revealed the existence of an expansive groundwater system throughout Taylor Valley (Mikucki *et al.* 2015)—the most historically well studied of the Dry Valleys. The presence of such a groundwater system transforms our understanding of hydrological connectivity throughout the valley, as subsurface water availability may regulate various biological systems, enhance the discharge of water and solutes into the McMurdo Sound (Foley *et al.* 2019), regulate geothermal heat flux rates (Foley *et al.* 2020) and influence surface hydrological connections.

To investigate whether similar groundwater systems exist in other regions of the McMurdo Dry Valleys, a second AEM campaign was flown in November 2018, with the objective of expanding AEM spatial coverage across the region (Fig. 1). In this paper, we focus on select locales, namely within the Wright and Garwood Valleys (Fig. 1, left-hand panel), where AEM data showed the presence of strong induced polarization (IP) effects. IP occurs when a part of the subsurface, instead of acting as an electrical resistor or conductor, behaves like a capacitor and stores and discharges electrical currents during EM soundings (Madden & Cantwell 1967), a process that can significantly perturb EM data. IP can limit or prevent the ability of traditional AEM inversion workflows to fit observed data,

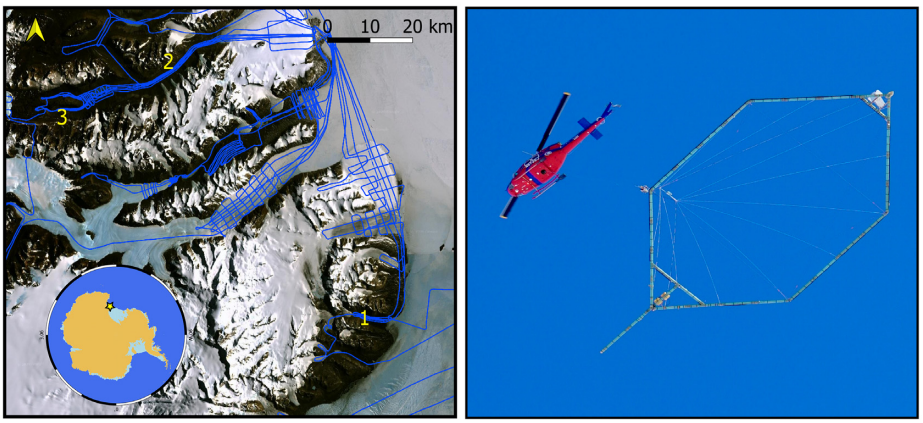

Figure 1. Left: an overview of the McMurdo Dry Valleys. The inset shows the location of the McMurdo Dry Valleys in Antarctica. Blue lines indicate the areas surveyed during the 2018 AEM campaign. Numbers indicate the examples discussed in the Results section: Garwood Valley (1), Wright Valley (2) and Don Juan Pond (3). Right: an image of the AEM system during flight.

greatly reducing the value of IP-affected data. However, valuable insights into subsurface geology can still be extracted (Kaminski & Viezzoli 2017; Viezzoli *et al.* 2017). To ensure reliable geological interpretations and data fits can be formed in the presence of IP, workflows explicitly handling these effects must be employed (Kratzer & Macnae 2012; Kwan *et al.* 2015; Kang *et al.* 2017).

Our objectives here are to (1) discuss the observation and characteristics of strongly IP-affected AEM data in the Wright and Garwood Valleys, and (2) highlight the key insights about regional hydrogeology and permafrost conditions that can be reliably extracted from IP-affected AEM data in similar settings. The presented examples exhibit three of the most common IP-affected AEM signatures—steeply dipping positive decays, decays containing sign changes and purely negative decays (Lee 1981; Flores & Peralta-Ortega 2009; Viezzoli & Manca 2020). These examples create scenarios where traditional workflows that do not account for IP effects either cannot fit the data or can only fit the data after aggressive data culling, where portions of the data are excluded from subsequent inversions.

BACKGROUND

Airborne transient electromagnetics

A transient electromagnetic (TEM) measurement involves driving a strong DC current in a large transmitter loop (Nabighian 1991). The current in the transmitter loop is then turned off as rapidly as possible to approximate a square wave, which generates a time-varying magnetic field in the subsurface during the current ramp-down. This time-varying magnetic field leads to the generation of electrical eddy currents in the subsurface, which in turn generate their own time-varying secondary magnetic field (Fitterman & Stewart 1986). The strength and time dependence of these secondary magnetic fields are then measured inductively by a receiver coil. In the case of AEM, both the transmitter and receiver coils are suspended beneath an aircraft, and AEM data collection occurs as the aircraft flies at speeds up to $\sim$100 km hr^{-1}. Typical AEM systems can penetrate to depths of several hundred metres, with penetration varying depending on the system and local conditions.

Raw AEM data consist of curves showing the time–magnitude relationship of the decaying eddy currents. Regions of the subsurface that are highly conductive give rise to larger amplitude, slowly decaying eddy currents, while poorly conducting regions give rise to weaker amplitude, fast decaying eddy currents. By observing the amplitude and time dependence of the induced eddy currents, information about the spatial distribution of electrical properties in the subsurface can be extracted. From images of electrical properties, one can infer the spatial extent/geometry and broad geologic types of materials (e.g. sand, permafrost, bedrock, bulk water content, etc.) of various hydrogeological units, as different hydrogeological units can often be differentiated based on contrasts in their electrical properties (Auken *et al.* 2017). Traditional AEM workflows involve inverting observed time–amplitude decay curves for images of resistivity—referred to in the following as a resistivity-only inversion. The fundamental assumption in these cases is that the various hydrogeological units behave purely as resistors.

IP in TEM data

In certain cases, the subsurface may behave like both a resistor and a capacitor, a phenomenon occurring when a process called IP allows hydrogeological units to be charged during the pulses and subsequently discharged after the completion of the primary EM pulse. In these cases, the subsurface resistivity is treated using a frequency-dependent complex-valued resistivity $\tilde{\rho}(\omega)$:

$$\tilde{\rho}(\omega) = \rho'(\omega) + i\rho''(\omega), \tag{1}$$

where ρ' and ρ'' represent the real and imaginary components of the complex-valued resistivity, respectively; i is the square root of -1; and ω is the angular frequency. The components ρ' and ρ'' are linked to bulk and surface conduction, respectively. The complex-valued resistivity is often described using the Cole–Cole model (Pelton *et al.* 1978):

$$\tilde{\rho}(\omega) = \rho_0 \left[1 - m_0\left(1 - \frac{1}{1 + (i\omega\tau_\rho)^C}\right)\right], \tag{2}$$

where ρ_0, m_0, τ_ρ and C are called the Cole–Cole parameters. In particular, ρ_0 and m_0 are the most commonly discussed and represent the amplitude of the direct current (i.e. 0 Hz) component of the complex-valued resistivity and the chargeability, respectively. In the limit that no IP effects are present (i.e. $m_0 = 0$), the complex-valued resistivity converges to the real-value, low-frequency limit of the resistivity, ρ_0—where the traditional treatment of the subsurface

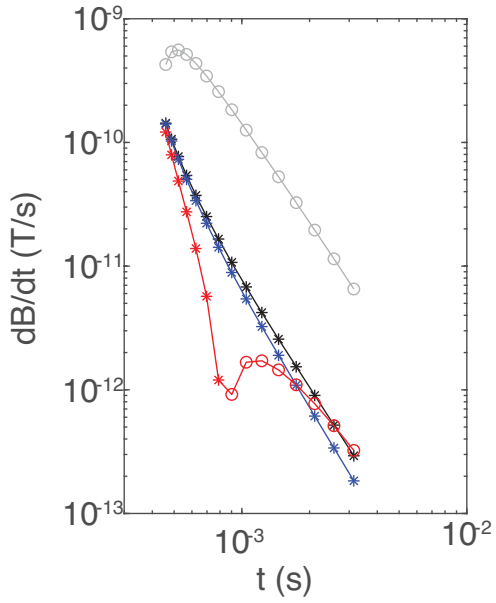

Figure 2. Example TEM decays for varying magnitudes of IP effects. The half-space properties underlying each curve are outlined in Table 1. Stars and open circles indicate positive and negative data points, respectively.

Table 1. Parameters used to produce the TEM decays in Fig. 1.

Profile colour	ρ_0 (Ω m)	φ_{max} (mrad)	τ_φ (s)	C (–)
Black	1000	–	–	–
Blue	1000	20	5e-4	0.5
Red	1000	100	5e-4	0.5
Grey	1000	500	5e-4	0.5

as a pure resistor is applicable. τ_ρ and C are terms controlling the location of the peak and width of the $\tilde{\rho}(\omega)$ spectrum in the frequency domain, respectively.

In this work, we use a re-parametrized version of the Cole–Cole model referred to as the maximum phase angle (MPA) approach (Fiandaca *et al.* 2018). The MPA approach has the benefit that its parametrization, where $\tilde{\rho}(\omega) = f(\rho_0, \varphi_{max}, \tau_\varphi, C)$, exhibits less correlation between each of the four underlying parameters than in the standard Cole–Cole model shown in eq. (2). The relationship between φ_{max}, τ_φ and the traditional Cole–Cole parameters is discussed in detail in Fiandaca *et al.* (2018). Of importance in this work is that the parameter φ_{max} can be considered to represent the relative strength of the IP phenomena—φ_{max} is linked to the ratio of surface and bulk conduction. Regions of the subsurface displaying large φ_{max} values (eg. $\varphi_{max} > 100$ mrad) correspond to areas where the IP effect is strong, and areas displaying small φ_{max} values correspond to regions where IP effects are weak (e.g. $\varphi_{max} < 10$ mrad).

Examples of potential impacts of IP on TEM decays are shown in Fig. 2, which illustrates several synthetic IP-affected TEM decays, produced using AarhusInv (Auken *et al.* 2015)—a geophysical modelling software. The decays are modelled for a system representative of the high-moment data collected using the same system used to collect the presented field data (Sørensen & Auken 2004). Four decay curves are illustrated for different homogeneous and isotropic half-space scenarios, where the properties of each half-space (curve colour) are listed in Table 1. The half-space parameters are selected to produce three types of IP-affected decays observed in the AEM data collected in the McMurdo Dry Valleys. The black line illustrates the response of a 1000 Ω m half-space, which does not have any IP effects, and represents the case where the subsurface behaves as a pure resistor. In this case the data has only a positive sign. The blue, red and grey lines illustrate IP-affected decays for increasing strength of the IP effects. The blue curve displays a more rapid decay than the zero-IP black curve, a feature often referred to as an 'oversteepening'—a decay that is too steep to be explained by a purely resistive subsurface. All data are still positive. The red line displays a sign change, highlighted by the switch from stars to open circles (i.e. positive to negative data points). The grey line displays negative data for the full decay. In real-world data, the characteristics of IP-affected decays will be determined by local subsurface properties, for example, local layering, resistivity and IP parameters.

The red, blue and grey curves (Fig. 2 and Table 1) represent very challenging scenarios for the traditional resistivity-only inversions to fit. For example, the blue curve is likely to be fitted by an overly resistive model (given its enhanced steepness), while the negative portions of the red and grey decays would have to be culled. This culling removes nearly half the red curve and the entirety of the grey curve. Furthermore, attempting to fit the positive portion of the red curve with a resistivity only inversion may yield resistivity values that differ from real in situ values.

Data collection and inversion

Data presented here were collected using the SkyTEM 312 system, a dual-moment system balancing large penetration depths with high resolution in the shallow subsurface. The high moment corresponds to a transmitter moment of 450 000 Am^2 with time gates ranging from 0.1 to 10.7 ms, while the low moment transmitter moment is 4100 Am^2 with time gates ranging from 0.02 to 1.4 ms (where time = 0 occurs at the end of the ramp). In this paper, only high-moment data is considered. For much of the investigated region (e.g. Wright and Victoria Valleys) the low-moment data was at the level of system noise and therefore culled. In Garwood Valley, low-moment data exceeded the system noise levels, but cannot be fit simultaneously with the high-moment data. The reason for the inability to fit both simultaneously is currently unknown, and high-moment data was prioritized as it displayed much higher signal-to-noise. Data were collected at flight speeds ranging from 80 to 120 km hr^{-1}, with the system altitude typically between 30 and 60 m above ground level. Data processing uses automatic filtering procedures that involve culling data exceeding a standard deviation threshold of 25 per cent the data value, as well as data that violate a filter focused on identifying oscillation from one time gate to the next. Manual processing was conducted after the automated protocols and was generally focused on culling data that were considered to be beneath the system noise floor determined from high-altitude flight tests—a test where data are collected at altitudes high enough to not be affected by the Earth response. The area is devoid of substantial human infrastructure and as such couplings are a non-issue throughout the valleys.

The IP inversion of AEM data in this work follows a similar workflow as that outlined by Couto Jr. *et al.* (2020). AEM data are inverted using the MPA-parametrization of the Cole–Cole model and a 1-D forward model, which requires that the data at each site be fit using a layered Earth model directly beneath the sounding location. Vertical and lateral constraints are imposed to stabilize the inversions and impose lateral smoothing both vertically and

along the flight line (Auken *et al.* 2005). The four parameters ρ, φ_{max}, τ_φ and C are bounded to range between [1e-1 2e4] Ω m, [1e-2 1e3] mrad, [1e-5 1e2] s, and [0.1 0.6] (unitless), respectively. Fixing τ_φ and C for initial model updates was observed to greatly improve convergence and stability versus an approach where these parameters are allowed to update during the first several iterations. Hence, they are held constant during the first 10 iterations. The depth discretization involves 30 layers with logarithmically increasing layer thicknesses, 4 m thickness of the first layer, and 500 m depth to the last layer. The depth of investigation (DOI) at each location is estimated based on the influence of the underlying subsurface on the observed data, and whether it affects the data to a degree greater than the noise level. Further information on DOI calculation is given in Christiansen & Auken (2012). In the following images, the inversion results are blanked (made semi-transparent) beneath the DOI.

Geological setting

The bedrock underlying Garwood Valley is composed of Skelton Group metasediments and igneous intrusives of Precambrian to Cambrian age (Dagel 1985). Bedrock in east-central Wright Valley consists of Precambrian to Palaeozoic metasediments, granite–gneisses, and lamprophyre and rhyolite porphyry dikes (Hall & Denton 2005). Surficial deposits in both valleys are dominantly glacial tills of various ages with alluvium proximal to streams (Hall & Denton 2005; Levy *et al.* 2017). The total thickness of frozen ground (permafrost) in the study region is variable depending on valley position. Typical thicknesses in the coastal region of Taylor Valley are 300–350 m (Decker & Bucher 1980), however temperatures at the depth of the freezing isotherm are often well below 0 °C because of the presence of brines in the subsurface (Decker & Bucher 1980; Mikucki *et al.* 2015). Active-layer (seasonal thaw) depths are 45–70 cm in coastal areas and in the eastern half of Wright Valley, and 20–45 cm in other ice-free areas within 60 km of McMurdo Sound (Bockheim *et al.* 2007). Garwood Valley has numerous ponds, especially near the coast. All pond bodies flown over at the time of this survey would have some component of liquid water within them, usually insulated below an ice cover of variable thickness (unpublished data).

RESULTS

Garwood Valley

Garwood Valley is a relatively ice-free coastal valley that terminates near the Koettlitz Glacier and the McMurdo Ice Shelf. It contains two small glaciers as well as several small ponds near the eastern end of the valley. Two larger ponds are also present further up-valley near the glaciers. Of interest, was the presence of a possible groundwater system running the length of the valley, the thickness of the permafrost layer, and the hydrological connectivity between the surface and subsurface.

The Garwood Valley flight line crosses the two glaciers as well as a pond near the west end of the valley (Fig. 3a). Towards the east end of the valley, the profile traverses several small ponds and terminates at the McMurdo Ice Shelf. Fig. 3(b) illustrates the data collected along the blue profile in Fig. 3(a), where the data in this case are all positive (blue dots). The transient electromagnetic sounding (dB/dt curve) at each location corresponds to a vertical line (Fig. 3b), where the y-axis shows the amplitude of the dB/dt data curve. Horizontal lines in Fig. 3(b) connect the same time gates for neighbuoring soundings. Fig. 3(b) is a convenient visualization of data collected along the flight direction, where lateral consistency can be identified by horizontal lines, while more local anomalies result in local maxima or minima. In this case, IP effects are not obvious from the data records—as no clear sign changes or negative values (red dots) are observed. Only after initial inversions using

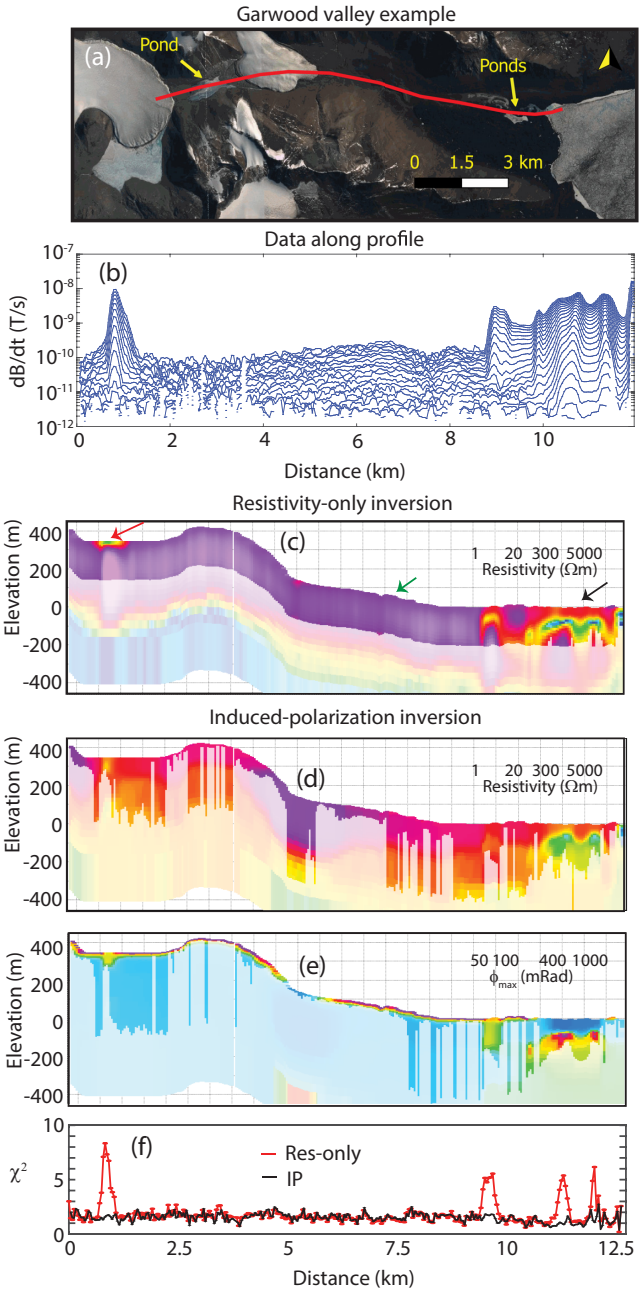

Figure 3. Results of an AEM survey in Garwood Valley. (a) Satellite image of Garwood Valley and the location of the relevant flight line (blue line). (b) TEM data collected along the flight line. Blue dots indicate positive-valued data. (c) A resistivity profile of the data in (b) produced by a resistivity-only inversion. (d) and (e) illustrate the resistivity and φ_{max} profiles produced by an IP inversion of the data in (b). (f) The red and black lines indicate the χ^2 (data fit) along the profile; the red and black lines correspond to the resistivity-only and IP inversions, respectively.

resistivity-only workflows are oversteepened curves readily identified near the fringes of the ponds (e.g. the steep anomalies near 1 and 9 km).

Fig. 3(c) shows the results of a resistivity only inversion of the data illustrated in Fig. 3(b). This image is called a resistivity profile and illustrates the estimate of the estimated electrical resistivity for a vertical slice into the subsurface. The *y*-axis corresponds to elevation in meters above sea level, while the *x*-axis corresponds to distance along the profile in kilometres. The left- and right-hand sides of the profiles corresponding to the western and eastern-most points of the profiles, respectively. The estimated resistivity at each location is illustrated by the colour scale, with low resistivities (equivalent to high conductivities) indicated with blue colours while more resistive regions correspond to purples. Local conductive anomalies are observed at locations where the profile intercepts known ponds, while stretches between ponds correspond to very resistive values and little structure (consistent light purple colours). The conductive anomalies extend to tens of meters beneath the pond bottoms and stretch laterally beyond the surficial edges of pond. The resistivity only inversion yields poor data fits over the local conductive anomalies—both the blue/green anomalies in the right-hand side of Fig. 3(c) as well as the shallow anomaly in the left-hand side of Fig. 3(c)—which can be seen by the peaks in the red data fit curve in Fig. 3(f). In the centre of the profile (purple region) the data is fit within error.

To improve the overall data-fit and ability to fit oversteepened decays near pond edges an IP inversion is also employed. Figs 3(d) and (e) illustrate the resistivity and φ_{max} profiles, respectively. The resistivity profile in this case displays fewer extreme values than those resulting from the resistivity-only inversion (Fig. 3c), with the central regions of the profile returning lower resistivities that further reduce with depth. The local low resistivity anomalies observed underneath the ponds are also thicker and have slightly higher resistivity values (e.g. the anomaly at 9.5 km in the resistivity only profile is significantly muted in the IP inversion) compared to Fig. 3(c). The φ_{max} profile displays a thin layer of elevated φ_{max} along the full extent of the valley, with high φ_{max} anomalies also appearing beneath the ponds. The black data fit curve in Fig. 3(f) highlights that the IP inversion provides a satisfactory data fit along the entire profile.

The two Garwood Valley resistivity profiles (Figs 3c and d) are similar in some respects. Both show regions of low resistivity beneath the low-elevation ponds near the coast (region near the black arrow in Fig. 3c). Such ponds in permafrost landscape are expected to be associated with taliks, which represent areas of unfrozen ground protected from freezing by the subsurface 'thermal shadows' of the surface lakes or ponds (O'Neill *et al.* 2020). This interpretation is more readily reconciled with the output of the IP inversion than the resistivity-only inversion since the latter inserts some very high resistivity regions right beneath the low resistivity water body. Similarly, at the right-hand side of the profile (close to the sound), the resistivity only inversion yields large spatial fluctuations in resistivity, from dozens of Ω m to thousands of Ω m, within a short vertical and horizontal distance. In contrast, the IP inversion produces more muted and gradual changes in resistivity in the same region, which we believe are more easily interpreted in terms of the expected thermal and hydrologic properties of the subsurface. The second pond area, in the upper part of the valley (region near red arrow in Fig. 3c), looks distinctly different in Figs 3(c) and (d). The resistivity-only inversion suggests that the upper pond is surrounded by a clearly defined thaw bulb (low resistivity, unfrozen ground) underlain by very high resistivity permafrost (thousands of Ω m). In contrast, the IP inversion indicates a small talik with modest resistivity (hundreds of Ω m). Furthermore, the two inversions also show a big difference in the resistivity of the permafrost layer between the lower and upper pond areas in Garwood Valley (region near green arrow in Fig. 3c). Whereas the resistivity-only inversion suggests a largely uniform high resistivity permafrost (thousands of Ω m), the IP inversion shows similarly high resistivity only in part of the profile with much of the permafrost imaged by this inversion having resistivities lower than 1000 Ω m. Although we do not have independent constraints on the subsurface of Garwood Valley, reconciling the IP-inversion profile with the expected thermal and hydrogeologic conditions, is a better fit than if the profile were derived using the resistivity-only inversion.

Wright Valley

At the eastern edge of Wright Valley is the Bowers Piedmont Glacier, with Lake Vanda, the largest lake in the McMurdo Dry Valleys, further up-valley (west of the left-most side of the image in Fig. 4a). The Onyx River runs through the centre of the east end of valley carrying meltwaters from the Bowers Piedmont Glacier to Lake Vanda. The valley floor is predominantly a mix of unconsolidated lacustrine sediments and glacial till of various ages which are distinguished by the amount and distribution of soluble salts and degree of chemical weathering (Bockheim & McLeod 2006). Surface expressions of bedrock are also present. Five AEM transects were flown through the Wright Valley, each displaying strong IP effects (Fig. 4a). Fig. 4(b) illustrates data for one of the flight lines (red line in 4A), the particular line is selected because it contains the most data post-culling and contains data representative of the other lines, which has both positive (blue) and negative (red) data. All three IP signatures are observed, including steeply dipping decays (at ∼22 km), sign changes (at ∼1–2 km), and fully negative decays (regions of only red data). Data gaps in Fig. 4(b) correspond to regions where the data were considered to have dropped beneath the noise floor of the instrument and has been culled. At a minimum, these regions can be considered to be very resistive or at least devoid of significant conductors within the depth of penetration. The up-valley sign change region (blue lobe near distances of 1 km in Fig. 4b) occurs near the intersection of Bull Pass and the Onyx River floodplain (highlighted by the red polygon in Fig. 4a) and corresponds to a local low in topography. In this case, much of the collected data are unusable by a resistivity-only workflow, as long-stretches of negative only data are present. As such, the ability of the IP inversion to handle negative data greatly increases useable data coverage in this area.

The Wright Valley resistivity and φ_{max} profiles (Figs 4c and d) along the blue line in Fig. 4(a) were produced using an IP inversion. The resistivity profile displays high-resistivity values for nearly the full length of the Wright Valley, with most resistivity values exceeding 500–1000 Ω m. A low-resistivity anomaly is observed in the left-hand side of the image, where the sign-change anomaly in Fig. 4(b) (red polygon in Fig. 4a) is present. For the φ_{max} profile (Fig. 4d), an elevated φ_{max} layer is observed at shallow depths. The depth of investigation in the φ_{max} profile is reduced for much of the valley compared to the resistivity profile. In the φ_{max} profile, an anomaly is observed at the same location as the low resistivity anomaly—again at the sign-change location in the left-hand side of Fig. 4(d). Taken together, the profiles indicate a consistently high resistivity and an absence of conductors—potentially indicative of paucity of liquid water to the penetration depth of the system for

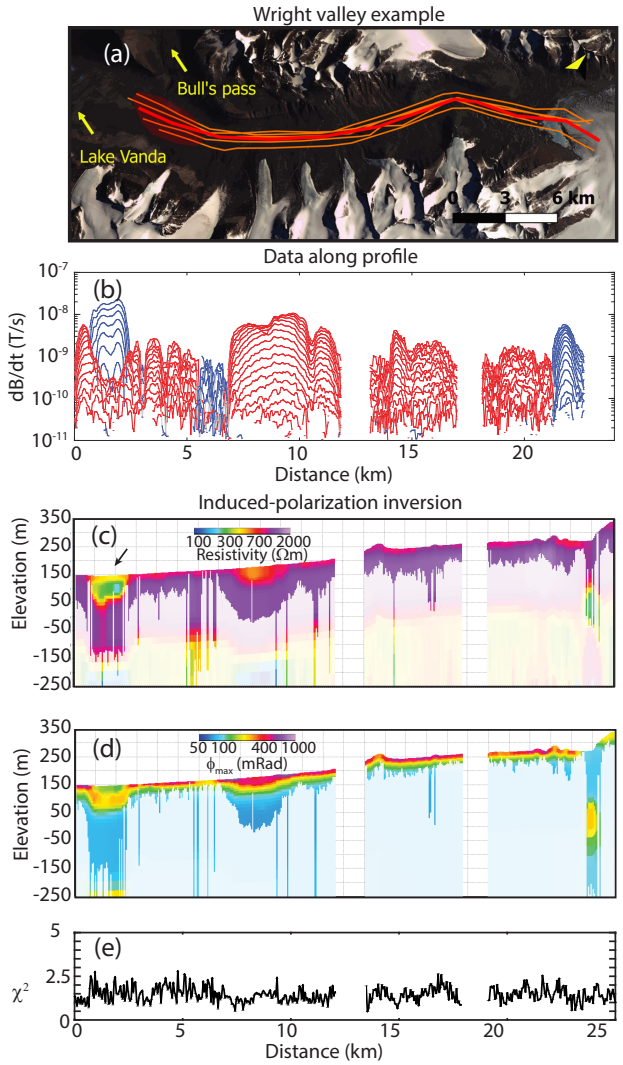

Figure 4. Results of an AEM survey along a line in Wright Valley. (a) Satellite image of Wright Valley and the location of the relevant flight line (blue line). Several other flight lines are illustrated by black lines. (b) The TEM data collected along the flight line. Blue and red dots indicate positive- and negative-valued data, respectively. (c) and (d) illustrate the resistivity and φ_{max} profiles produced by an IP inversion of the data in (b). Note that in all panels moving from left to right corresponds to moving from west to east. (e) The χ^2 (data fit) along the profile corresponding to the inversion results in (c) and (d).

much of the valley. All other flight lines in Wright Valley display inversion results consistent with Fig. 4.

The conductive and high φ_{max} anomalies occurring at depth (e.g. black arrow near ∼2 km in Fig. 4c) are interpreted to be locations in the valley floor where cryoconcentrated brines accumulated. We discount the possibility that subsurface liquid water is fresh based on the observation that the McMurdo Dry Valleys have abundant brines in the subsurface, and even in the surface lakes, including Lake Vanda (Mikucki *et al.* 2015; Dugan *et al.* 2015; Foley *et al.* 2016). To remain liquid at expected subsurface temperatures the brines would also have to be of elevated salinity. Inversions of other Wright Valley lines display profiles consistent with Fig. 4. These brines are possibly from small amounts of meltwater and dissolution of salts present in soils, which have collected over time in the shallow part of the permafrost layer. Such features, formed where high salinity enables near-surface brines to stay unfrozen even when surface temperatures are as low as in this region (*ca.* −20 °C) are referred to as cryopegs (O'Neill *et al.* 2020). These near-surface features are distinctly different from the deep brine-bearing aquifers discovered previously in Taylor Valley (Mikucki *et al.* 2015), suggesting that the two neighbouring valleys are hydrologically quite different. Features such as these, where local lows in topography are observed to produce data signatures described by a transition from full-negative decays, to decays with sign changes, and back to full-negative decays as one traverses a local topography low are seen at several locations in the Wright Valley (e.g. in the North Fork of the Wright Valley north of Don Juan Pond, west of Lake Vanda, but is not visible in Fig. 4). We believe this to be a result of topographic lows causing local differences in the subsurface brine content compared to the regional setting.

Don Juan Pond

Don Juan Pond is a hyper-saline pond located in the Wright Valley, and is currently the second saltiest body of water on Earth. The pond is approximately 400 m long by 100 m wide with an average depth of ∼10 cm. The extremely high salt concentration allows the pond to remain unfrozen down to temperatures of −52 °C (Marion 1997)—leaving the pond unfrozen through the cold Antarctic winter. Detailed tables of brine concentrations are given in Toner *et al.* 2017. The source of the highly concentrated calcium chloride brine has been debated for decades, with proposed sources as both deep groundwater (Harris & Cartright 1981; Toner *et al.* 2017) and surface deliquescence (Dickson *et al.* 2013). Borehole investigations in the 1960s did reveal saline groundwater beneath the pond (Harris & Cartright 1981). To explore the extent of this groundwater system and any valley-wide subsurface connections with Lake Vanda, several AEM lines were flown over the pond and the neighbouring valley sections. Fig. 5(a) illustrates a satellite image of the pond, where the blue line indicates one of the four AEM lines traversing the pond. A rock glacier can be seen to the west of the pond, while Lake Vanda is about 10 km down valley (to the upper right corner of the image). Fig. 5(b) illustrates AEM data along the blue line in Fig. 5(a), where positive data are observed over the pond and pond edges, with a transition to purely negative decays further down valley (to the right in Fig. 5a), similar to the feature observed in the red polygon in Fig. 4(a). Note that a resistivity only inversion would require much more aggressive data culling to produce satisfactory data fits in this scenario, as much of the eastern portion of the profile (negative data section) would have to be discarded.

Figs 5(c) and (d) illustrate the resistivity and φ_{max} profiles produced from an IP inversion of the data in Fig. 5(b). The pond is identified as the low resistivity anomaly (blue colours) near the 2 km mark, with high resistivity zones to the east (rock glacier) and west of the pond. Beneath the pond, a low resistivity zone appears to extend 10s of meters beneath the pond with a gradual transition towards higher resistivities with depth. This zone (yellows/oranges) appears to extend laterally away from the pond edges stretching underneath the rock glacier and extending further down valley. φ_{max} anomalies coincident with the low-resistivity values underneath the pond are also observed. An elevated φ_{max} layer at shallow depths is also observed to the east and west of the pond, in a similar fashion as was seen in the previous Wright Valley example. This shallow elevated φ_{max} layer was again interpreted to correspond to a chargeable layer at the top of the permafrost where small volume

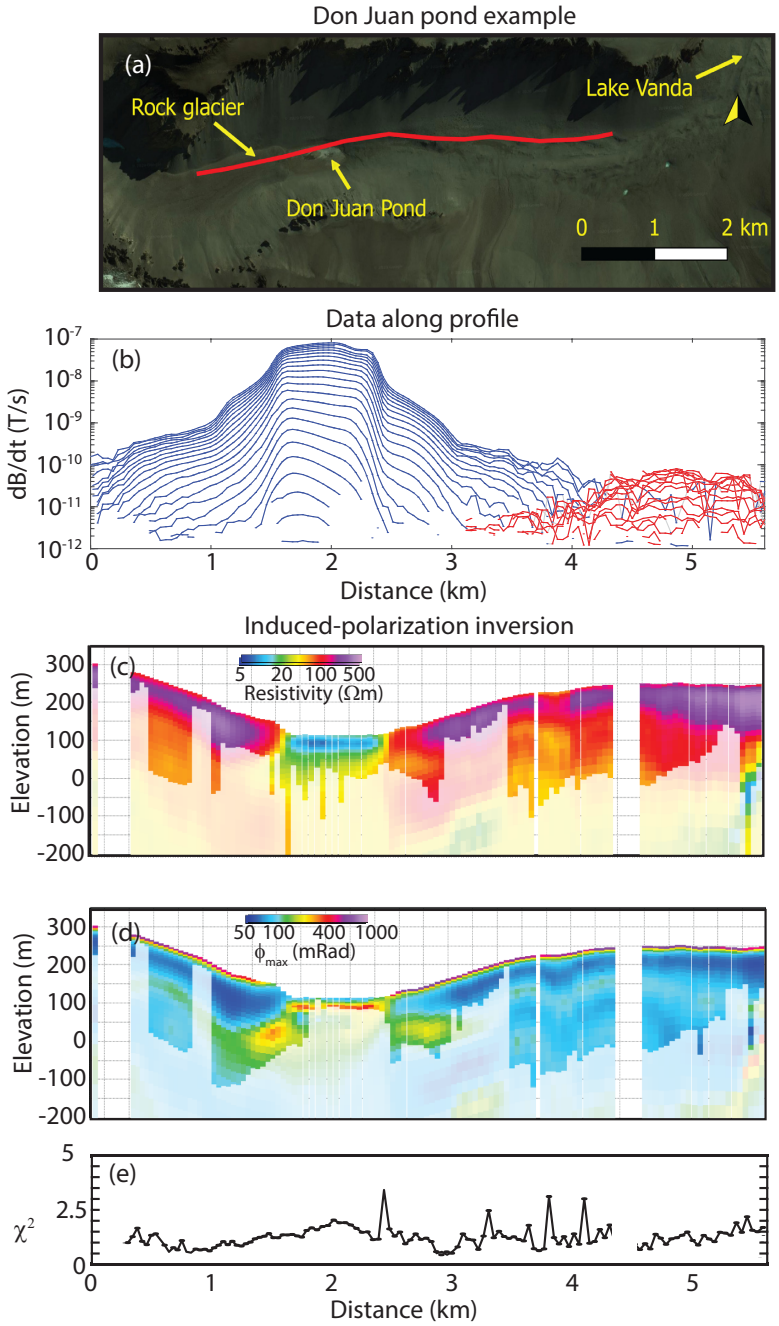

Figure 5. Results of an AEM survey traversing Don Juan Pond. (a) Satellite image of Don Juan Pond and the location of the relevant flight line (blue line). (b) The TEM data collected along the flight line. Blue and red dots indicate positive- and negative-valued data, respectively. (c) and (d) illustrate the resistivity and φ_{max} profiles produced by an IP inversion of the data in (b). Note that in all panels moving from left to right corresponds to moving from west to east. (e) The χ^2 (data fit) along the profile corresponding to the inversion results in (c) and (d).

fraction of hyperconcentrated brine may be occupying void space in the permafrost layer. An electrical resistivity tomography survey conducted near the pond in the 1970s also agrees well with the structures observed in Fig. 5(c) (McGinnis *et al.* 1973).

DISCUSSION

Airborne time-domain electromagnetics is a powerful tool for regional hydrogeological investigations. In the McMurdo Dry Valleys, AEM is particularly well suited to imaging regional groundwater systems and the conditions at the base of glaciers. The frozen environment leads to strong contrasts in electrical properties between various layers—for example, conductive brines at the base of very resistive glacier ice—or liquid groundwater underneath a confining permafrost layer. These strong resistivity contrasts make for attractive AEM imaging targets. AEM is likely to have similar utility in other polar regions and for applications interested in mapping the spatial extent of liquid water in a frozen substrate. Another valuable feature of AEM is its minimal impact on environmentally fragile landscapes and its ability to image over rugged terrain, as the system is suspended during measurement and no persons are required on

the ground in the surveyed areas—only at the launch and landing points. As such, this tool is well suited for difficult to access or dangerous terrain such as glaciers.

One consistent feature for the IP-affected data in the presented examples is the presence of a high-resistivity background, for example, the fringes of Don Juan Pond, or much of the Wright and Garwood Valleys. The very resistive background effectively accentuates the IP response of the Earth—that is, the traditional electromagnetic response of the Earth, where the Earth behaves purely as a resistor, is so small that IP effects can become the dominant feature of the observed signals. This can be understood by considering a simplified model where the Earth's response is described by a resistor and capacitor in parallel (the traditional and IP part, respectively). By reducing the resistor's signal, the relative contribution of the capacitive response grows. If the background resistivity were lowered, it may become more difficult to identify IP effects, as the relative contribution of the capacitive signal to the total observed signal is reduced. This could explain why no obvious IP-affected data are observed in other regions of the McMurdo Dry Valleys (not shown)—such as the Taylor Valley, where the background resistivity is lower due to a regional groundwater system and the traditional resistivity only inversions are able to provide satisfactory data fits.

Several mechanisms can lead to IP responses in electromagnetic data. Most commonly, strong IP affects are observed in large proportions of clay but where clay is the non-dominant phase (Marshall & Madden 1959; Olhoeft 1985; Levy *et al.* 2018). The plate-like structures in the clay matrix can lead to strong polarization/charge gathering and subsequent discharge. However, clays are not expected to be the major source of IP effects in the McMurdo Dry Valleys as the prevailing depositional environments and weathering conditions form clay-poor sediments (Campbell & Claridge 1987). Another possible source of IP effects could be the presence of mineralization. Tamppari *et al.* (2012) observed minerals such as Ferric iron, iron oxides and pyrite in neighbouring Taylor Valley—all materials that may lead to IP effects in a highly resistive background. However, a borehole drilled in the vicinity of Don Juan Pond displayed a sequence consisting of ∼12 m of silty-sandy sediments overlying about 50 m of a fractured Ferrar diabase with a crystalline basement underneath. The geologic borehole logs (Mudrey *et al.* 1975) note only mineralization with calcite and, locally, adularia, neither of which can explain the conductive and chargeable subsurface. If the local anomalies in Figs 4 and 5 are due to mineralizations, it would be a significant coincidence that they correspond to the modern locations of Don Juan Pond and local topographic depressions. The regional continuity of the Ferrar Dollerite sill, which is present in the vicinity of Don Juan Pond and beyond, also suggests that local mineralizations associated with this subvolcanic rock would be unlikely. We conjecture that the geometry and spatial context of the observed deep IP effects, such as their presence underneath Don Juan Pond and in topographic lows are more compatible with a hydrogeologic explanation of their origin, but a mineralization explanation cannot be fully ruled out.

A potential source of the observed IP effects is the Maxwell–Wagner effect occurring at the ice–rock interface (Zorin & Ageev 2017). The Maxwell–Wagner effect describes the accumulation of charges at the interface between mixed materials when current flows across the interface. Kozhevnikov & Antonov (2012) highlight the consistency between ground-based TEM data collected in permafrost regions and behaviour expected from Maxwell–Wagner effects. IP effects in AEM have also been previously reported in permafrost regions by Smith & Klein (1996). Another possible IP source could be diffusion-controlled polarization occurring at the electrical double layer (Binley & Slater 2020). Both mechanisms are consistent with the decay rates displayed by observed IP anomalies.

The two types of IP anomalies observed in Figs 3–5—manifest either as an elevated φ_{max} layer at shallow depths present in a highly resistive background or as an anomaly at depth described by a locally elevated φ_{max} and low resistivity—both occur in situations where there is likely to be unfrozen water. At shallow depths, recharging meltwaters are likely to lead to residual unfrozen water content. Such shallow waters may have high salinity given that soils in the region contain abundant salts (Bockheim & McLeod 2006). As the subsurface freezes, a residual film of unfrozen water coats the grain/ice interface while ice forms in the interior of pores (Kleinberg & Griffin 2005). Additionally, it is long known that electrolytic conduction is enhanced near charged solid boundaries (Smoluchowski 1917); under such conditions, the complex resistivity becomes increasingly dominated by surface conduction (i.e. the imaginary part of the complex resistivity) as bulk conduction (the real component of the complex resistivity) becomes less effective (eq. 1). This causes a locally elevated φ_{max} that appears visually as the shallow high φ_{max} in Figs 3–5. For the IP anomalies observed at depth, these features tend to coincide with taliks (as in the Wright and Garwood Valleys) or locations of suspected groundwater systems (as at Don Juan Pond) where unfrozen water is likely present at depth. Similarly to the shallow scenario, the unfrozen waters likely lead to an increased relative contribution of surface conduction—resulting in the appearance of the high φ_{max} at depth. We conjecture that these deep sources of high φ_{max} are associated with brines hosted in bedrock fractures, with relatively high surface-to-volume ratios, which may make surface conduction detectable even in the presence of significant bulk conduction. This conjecture is supported by the observation that the highest φ_{max} beneath Don Juan Pond does not occur in the sediment layer underlying the pond but at depths corresponding to the bedrock units found through past drilling (Mudrey *et al.* 1975).

The presented examples also highlight the ability of IP inversions to enhance the value of IP-affected AEM resistivity profiles. For example, all negative data regions in the Wright Valley and Don Juan Pond examples would be culled if traditional resistivity-only protocols were employed—as negative data cannot be fitted by resistivity-only inversions. Estimates of subsurface resistivity in these regions would not be available, and at best one could only make a qualitative estimate that the subsurface is likely to be in the high-resistivity limit—or at least have an absence of strong conductors. Furthermore, regions of sign change and oversteepening would also require aggressive data culling where negative data and late time gates would likely be culled because of an inability to fit the late gates of a steeply dipping decay. Such culling reduces data coverage and depth penetration. Although aggressive culling of IP effects may allow a resistivity-only inversion to provide a satisfactory data fit and salvage some IP-affected data, this approach is not optimal. This may lead to introduction of potentially spurious features and contains some logical inconsistency. Culling IP-affected data is an acknowledgement of IP's presence, yet selecting a resistivity-only inversion scheme assumes that IP is not present or negligible. While it may be that IP affects a limited portion of the decay curve, an inherent uncertainty is added about whether or not the remaining data contain subtle IP effects that may introduce artefacts.

The employed IP inversion involves estimation of four IP parameters. The presented field results display ρ and φ_{max} profiles, but not τ_{φ} and C profiles. In practice, ρ and φ_{max} (or ρ and chargeability for the IP inversions employing the standard Cole–Cole model) are generally treated as the most geologically informative profiles. In

this work, the inversion scheme involves holding τ_φ and C constant during the first 10 iterations of the inversion—a process that was observed to greatly improve convergence. When τ_φ and C were allowed to vary along with ρ and φ_{max} from the first iteration, convergence rates were slowed and in many cases the inversion failed to converge to a satisfactory data fit. The underlying τ_φ and C profiles in these four examples display little structure and often do not diverge far from the starting model values. Furthermore, the τ_φ and C profiles also often exhibit much shallower DOI than ρ and φ_{max}.

Note that any electromagnetic method conducted in these environments is susceptible to the influence of IP, including both frequency-domain and time-domain measurements. For example, several ground-based electromagnetic measurements conducted in the McMurdo Dry Valleys during this study (not shown here) also display IP effects.

CONCLUSIONS

AEM methods are powerful tools for geological characterization in polar environments. An AEM survey flown in the McMurdo Dry Valleys revealed that vast regions in the area display significant IP effects—effects of such a magnitude that traditional resistivity-only AEM inversion workflows are unable to fit observed data. In these scenarios, IP effects can render data useless—greatly reducing the value of AEM data for geological characterization. To enhance data value, a scheme for inverting IP-affected AEM data that directly accounts for IP effects may be employed. The scheme involves estimating the spatial variability of four parameters in the MPA re-parametrized Cole–Cole model. The presented results highlight that AEM data displaying oversteepened decays, sign changes and negative data can all be fit using this approach, and valuable insights into subsurface geology can be formed—regardless of the presence of IP effects. The ability to handle negative and oversteepened data greatly enhanced usable data coverage—particularly in the Wright Valley where purely negative data were observed over continuous stretches as long as dozens of kilometres.

The IP-affected regions in the McMurdo Dry Valleys tend to display IP anomalies in two different settings: a shallow strong IP layer present in a highly resistive background and an IP anomaly present at depth in coincidence with an area of lower resistivity. Both settings are likely to be associated with regions of locally elevated unfrozen water content, which likely gives rise to an increase in the importance of surface conduction. Consequently, the resulting IP anomalies in these settings may offer insights into the presence of unfrozen water.

ACKNOWLEDGEMENTS

This work was supported by funding from the NSF, Grant Nos. 1644187 to ST and 1643687 to JAM. We are thankful to SkyTEM Surveys ApS for helping us with the system deployment and support and to Lars Jensen in particular for his invaluable help. Without Lars this would not have been possible. We are also thankful for the logistical field support from the United States Antarctic Program, which enabled collection of our data. In particular, we thank the helicopter crews from PHI Inc. as well as the McMurdo helicopter coordinator Lindsay Steinbauer and her team. Our remote field data collection would not be possible without the capable help of our field support leader, Robin Carroccia, and without the aid from operators of the Marble Point refuelling station.

DATA AVAILABILITY

The data in this manuscript are available via the United States Antarctic Program Data Center. The direct link is https://www.usap-dc.org/view/dataset/601373.

REFERENCES

Auken, E., Christiansen, A.V., Jacobsen, B.H., Foged, N. & Sørensen, K.I., 2005. Piecewise 1D laterally constrained inversion of resistivity data, *Geophys. Prospect.,* **53**(4), 497–506.

Auken, E. *et al.*, 2015. An overview of a highly versatile forward and stable inverse algorithm for airborne, ground-based and borehole electromagnetic and electric data, *Explor. Geophys.,* **46**(3), 223–235.

Auken, E., Boesen, T. & Christiansen, A.V., 2017. A review of airborne electromagnetic methods with focus on geotechnical and hydrological applications from 2007 to 2017, *Adv. Geophys.,* **58,** 47–93.

Binley, A. & Slater, L., 2020. *Resistivity and Induced Polarization: Theory and Applications to the Near-Surface Earth*. Cambridge Univ. Press.

Bockheim, J.G. & McLeod, M., 2006. Soil formation in Wright Valley, Antarctica since the late Neogene, *Geoderma,* **137,** 109–116.

Bockheim, J.G., Campbell, I.B. & McLeod, M., 2007. Permafrost distribution and active-layer depths in the McMurdo Dry Valleys, Antarctica, *Permafrost Periglacial Process.,* **18**(3), 217–227.

Campbell, I.B. & Claridge, G.G.C., 1987. *Antarctica: Soils, Weathering Processes and Environment*. Elsevier.

Christiansen, A.V. & Auken, E., 2012. A global measure for depth of investigation, *Geophysics,* **77**(4), WB171–WB177.

Couto, M.A., Jr., Fiandaca, G., Maurya, P.K., Christiansen, A.V., Porsani, J.L. & Auken, E., 2020. AEMIP robust inversion using maximum phase angle Cole–Cole model re-parameterisation applied for HTEM survey over Lamego gold mine, Quadrilátero Ferrífero, MG, Brazil, *Explor. Geophys.,* **51**(1), 170–183.

Dagel, M.A., 1985, Stratigraphy and chronology of stage 6 and 2 glacial deposits, Marshall Valley, Antarctica, *Master's thesis,* University of Maine, Orono, Maine, 75pp.

Decker, E.R. & Bucher, G.J., 1980. Geothermal studies in the Ross Island–Dry Valley region, in *Antarctic Geoscience,* ed. Craddock, C., University of Wisconsin Press.

Dickson, J.L., Head, J.W., Levy, J.S. & Marchant, D.R., 2013. Don Juan Pond, Antarctica: near-surface $CaCl_2$–brine feeding Earth's most saline lake and implications for Mars, *Sci. Rep.,* **3**(1), 1–8.

Doran, P.T., McKay, C.P., Clow, G.D., Dana, G.L., Fountain, A.G., Nylen, T. & Lyons, W.B., 2002. Valley floor climate observations from the McMurdo Dry Valleys, Antarctica, 1986–2000, *J. geophys. Res.,* **107**(D24), ACL 13–1-ACL 13-12.

Dugan, H.A., Doran, P.T., Tulaczyk, S., Mikucki, J.A., Arcone, S.A., Auken, E., Schamper, C. & Virginia, R.A., 2015. Subsurface imaging reveals a confined aquifer beneath an ice-sealed Antarctic lake, *Geophys. Res. Lett.,* **42**(1), 96–103.

Fiandaca, G., Madsen, L.M. & Maurya, P.K., 2018. Re-parameterisations of the Cole–Cole model for improved spectral inversion of induced polarization data, *Near Surf. Geophys.,* **16**(4), 385–399.

Fitterman, D.V. & Stewart, M.T., 1986. Transient electromagnetic sounding for groundwater, *Geophysics,* **51**(4), 995–1005.

Flores, C. & Peralta-Ortega, S.A., 2009. Induced polarization with in-loop transient electromagnetic soundings: a case study of mineral discrimination at El Arco porphyry copper, Mexico, *J. Appl. Geophys.,* **68**(3), 423–436.

Foley, N., Tulaczyk, S., Auken, E., Schamper, C., Dugan, H., Mikucki, J., Virginia, R. & Doran, P., 2016. Helicopter-borne transient electromagnetics in high-latitude environments: an application in the McMurdo Dry Valleys, Antarctica, *Geophysics,* **81**(1), WA87–WA99.

Foley, N. *et al.*, 2019. Evidence for pathways of concentrated submarine groundwater discharge in east Antarctica from helicopter-borne electrical resistivity measurements, *Hydrology,* **6**(2), 54.

Foley, N. *et al.*, 2020. Mapping geothermal heat flux using permafrost thickness constrained by airborne electromagnetic surveys on the western coast of Ross Island, Antarctica, *Explor. Geophys.,* **51**(1), 84–93.

Gooseff, M.N., Barrett, J.E. & Levy, J.S., 2013. Shallow groundwater systems in a polar desert, McMurdo Dry Valleys, Antarctica, *Hydrogeol. J.,* **21**(1), 171–183.

Hall, B.L. & Denton, G.H., 2005. Surficial geology and geomorphology of eastern and central Wright Valley, Antarctica, *Geomorphology,* **64,** 25–65.

Harris, H.J.H. & Cartwright, K., 1981. Hydrology of the Don Juan Basin, Wright Valley, Antarctica , *Dry Valley Drill. Proj. Bull.,* **33,** 161–184.

Kaminski, V. & Viezzoli, A., 2017. Modeling induced polarization effects in helicopter time-domain electromagnetic data: field case studies, *Geophysics,* **82**(2), B49–B61.

Kang, S., Fournier, D. & Oldenburg, D.W., 2017. Inversion of airborne geophysics over the DO-27/DO-18 kimberlites—Part 3: induced polarization, *Interpretation,* **5**(3), T327–T340.

Kleinberg, R. L. & Griffin, D. D., 2005. NMR measurements of permafrost: unfrozen water assay, pore-scale distribution of ice, and hydraulic permeability of sediments, *Cold Reg. Sci. Technol.,* **42**(1), 63–77.

Kozhevnikov, N.O. & Antonov, E.Y., 2012. Fast-decaying inductively induced polarization in frozen ground: a synthesis of results and models, *J. Appl. Geophys.,* **82,** 171–183.

Kratzer, T. & Macnae, J.C., 2012. Induced polarization in airborne EM, *Geophysics,* **77**(5), E317–E327.

Kwan, K., Prikhodko, A., Legault, J.M., Plastow, G., Xie, J. & Fisk, K., 2015. Airborne inductive induced polarization chargeability mapping of VTEM data, *ASEG Extended Abstr.,* **2015**(1), 1–5.

Lee, T., 1981. Transient electromagnetic response of a polarizable ground, *Geophysics,* **46**(7), 1037–1041.

Levy, J.S., Rittenour, T.M., Fountain, A.G. & O'Connor, J.E, 2017. Luminescence dating of paleolake deltas and glacial deposits in Garwood Valley, Antarctica: Implications for climate, Ross ice sheet dynamics, and paleolake duration, *GSA Bulletin,* **129**(9–10), 1071–1084.

Lévy, L., Gibert, B., Sigmundsson, F., Flóvenz, Ó.G., Hersir, G.P., Briole, P. & Pezard, P.A., 2018. The role of smectites in the electrical conductivity of active hydrothermal systems: electrical properties of core samples from Krafla volcano, Iceland, *Geophys. J. Int.,* **215**(3), 1558–1582.

Madden, T.R. & Cantwell, T., 1967. Part D: induced polarization. A review, *Min. Geophys.,* **2,** 373–400.

Marchant, D.R. & Head, J.W., III, 2007. Antarctic dry valleys: microclimate zonation, variable geomorphic processes, and implications for assessing climate change on Mars, *Icarus,* **192**(1), 187–222.

Marion, G.M., 1997. A theoretical evaluation of mineral stability in Don Juan Pond, Wright Valley, Victoria Land, *Antarct. Sci.,* **9**(1), 92–99.

Marshall, D.J. & Madden, T.R., 1959. Induced polarization, a study of its causes, *Geophysics,* **24**(4), 790–816.

McGinnis, L.D., Nakao , K. & Clark, C.C., 1973. Geophysical identification of frozen and unfrozen ground, Antarctica, in *Permafrost: North American Contribution to the Second International Conference,* Washington DC, pp. 136–146.

Mikucki, J.A. *et al.*, 2015. Deep groundwater and potential subsurface habitats beneath an Antarctic dry valley, *Nat. Commun.,* **6**(1), 1–9.

Mudrey, M.G., Torii, T. & Harris, H., 1975. Geology of DVDP 13: Don Juan Pond, Wright Valley, Antarctica, *Dry Valleys Drill. Proj. Bull.,* **5,** 78–93.

Nabighian, M. N., 1991. *Electromagnetic Methods in Applied Geophysics: Volume 2, Application, Parts A and B,* Society of Exploration Geophysicists.

Olhoeft, G.R., 1985. Low-frequency electrical properties, *Geophysics,* **50**(12), 2492–2503.

O'Neill, H.B., Roy-Leveillee, P., Lebedeva, L. & Ling, F., 2020. Recent advances (2010–2019) in the study of taliks, *Permafrost Periglacial Process.,* **31,** 346–357.

Pelton, W.H., Ward, S.H., Hallof, P.G., Sill, W.R. & Nelson, P.H., 1978. Mineral discrimination and removal of inductive coupling with multifrequency IP, *Geophysics,* **43**(3), 588–609.

Smith, R.S. & Klein, J., 1996. A special circumstance of airborne induced-polarization measurements, *Geophysics,* **61**(1), 66–73.

Smoluchowski, M., 1917. Versuch einer mathematischen Theorie der Koagulationskinetik kolloider Lösungen, *Z. Phys. Chemie,* **92,** 129–168.

Sørensen, K.I. & Auken, E., 2004. SkyTEM—a new high-resolution helicopter transient electromagnetic system, *Explor. Geophys.,* **35**(3), 191–199.

Tamppari, L.K. *et al.*, 2012. Effects of extreme cold and aridity on soils and habitability: McMurdo Dry Valleys as an analogue for the Mars Phoenix landing site, *Antarct. Sci.,* **24**(3), 211.

Toner, J.D., Catling, D.C. & Sletten, R.S., 2017. The geochemistry of Don Juan Pond: evidence for a deep groundwater flow system in Wright Valley, Antarctica, *Earth planet. Sci. Lett.,* **474,** 190–197.

Viezzoli, A. & Manca, G, 2020. On airborne IP effects in standard AEM systems: tightening model space with data space, *Explor. Geophys.,* **51**(1), 155–169.

Viezzoli, A., Kaminski, V. & Fiandaca, G., 2017. Modeling induced polarization effects in helicopter time domain electromagnetic data: synthetic case studies, *Geophysics,* **82**(2), E31–E50.

Zorin, N. & Ageev, D., 2017. Electrical properties of two-component mixtures and their application to high-frequency IP exploration of permafrost, *Near Surf. Geophys.,* **15**(6), 603–613.